Available online at www.sciencedirect.com

ScienceDirect

journal homepage: www.elsevier.com/locate/he

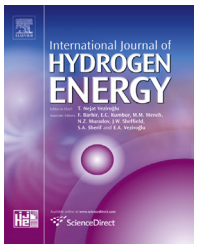

Numerical modeling of liquid water motion in a polymer electrolyte fuel cell

Fangming Jiang [a,b,*], *Chao-Yang Wang* [b]

[a] *Laboratory of Advanced Energy Systems, CAS Key Laboratory of Renewable Energy, Chinese Academy of Sciences (CAS), Guangzhou 510640, China*

[b] *Electrochemical Engine Center (ECEC), Department of Mechanical and Nuclear Engineering, The Pennsylvania State University, University Park, PA 16802, USA*

ARTICLE INFO

Article history:
Received 24 June 2013
Received in revised form
13 October 2013
Accepted 20 October 2013
Available online 22 November 2013

Keywords:
Polymer electrolyte fuel cell
Computational fuel cell dynamics
Multiphase mixture model
Water management

ABSTRACT

A three dimensional transient model fully coupling the two phase flow, species transport, heat transport, and electrochemical processes is developed to investigate the liquid water formation and transport in a polymer electrolyte fuel cell (PEFC). This model is based on the multiphase mixture (M2) formulation with a complete treatment of two phase transport throughout the PEFC, including gas channels, enabling modeling the liquid water motion in the entire PEFC. This work particularly focuses on the liquid water accumulation and transport in gas channels. It is revealed that the liquid water accumulation in gas channels mainly relies on three mechanisms and in the anode and cathode may rely on different mechanisms. The transport of liquid water in the anode channel basically follows a condensation–evaporation mechanism, in sharp contrast to the hydrodynamic transport of liquid water in the cathode channel. Liquid water in the cathode channel can finally flow outside from the exit along with the exhaust gas. As the presence of liquid water in gas channels alters the flow regime involved, from the single phase homogeneous flow to two phase flow, the flow resistance is found to significantly increase.

1. Introduction

Two-phase flow is ubiquitous in polymer electrolyte fuel cells (PEFCs). Optical visualization experiments [1–5] have corroborated the existence of liquid water not only in the PEFC cathode, but also in the anode. Having suitable amount of liquid water remain in electrodes may be favorable to the cell performance as it improves the membrane ionic transport capability. However, liquid water remaining in catalyst layers (CL) can cover the active reaction sites and that in porous diffusion media can block the pathways of reactants, leading to reduction of cell performance or even shutdown, referred to flooding. Flooding may also occur in gas channels if liquid water accumulates in and blocks the flow path. Besides deteriorated cell performance, flooding can also bring detrimental impact at the PEFC durability as it may cause fuel starvation and ensuing carbon corrosion [6,7], resulting in accelerated aging of the membrane electrode assembly (MEA). In addition, for a PEFC stack, channel flooding (or clogging) causes flow maldistribution, and thus leads to a non-uniform, cell-to-cell reactant distribution, further exacerbating flooding effects. Therefore, water management, aiming to balance the hydration of membrane with the avoidance of flooding, plays a pivotal role to ensuring high performance and long durability of PEFCs.

Understanding the distribution and transport of liquid water is the key to PEFC water management. While

* *Corresponding author*. Laboratory of Advanced Energy Systems, CAS Key Laboratory of Renewable Energy, Chinese Academy of Sciences (CAS), Guangzhou 510640, China.
E-mail addresses: fm_jiang2013@yahoo.com, fm_jiang2000@yahoo.com (F. Jiang).

0360-3199/$ – see front matter
http://dx.doi.org/10.1016/j.ijhydene.2013.10.113

considerable research efforts [8–13] have been expended to delineate the two phase transport in porous diffusion media and its impact on cell performance, the two-phase flow in gas channels remains intractable until a few years ago [14,15]. Almost all the mathematical modeling works [8–13] that were based on the M2 formulation [16] have an assumption of homogeneous mist flow in PEFC gas channels thereby no virtually informative results about the two phase flow in gas channels could be given. Wang et al. [14] first extended the M2 formulation to model the two phase flow in PEFC gas channels by taking the mini-channels as structured and ordered porous media. This concept was later deployed to deal with the two phase flow maldistribution in multiple gas channels of a PEFC stack by Basu et al. [15]. Another representative category of PEFC two phase flow models is the two-fluid model [17–22], which either adopts the unsaturated flow theory and solves liquid-phase equations only [17] or solves the gas-phase and liquid-phase equations [18–20] separately with some phenomenological approximations, e.g. drag and lift force [19], being introduced to account for the complex interactions between phases. The M2 model is more advantageous over the two-fluid model at computational efficiency due to much fewer primary variables involved and its capability of capturing the three dimensional dry–wet–dry transition [12] without tracking the multiple interfaces between single- and two-phase regions. The volume of fluid (VOF) method has also been used to simulate the two phase flow in PEFC air channel [23] and to investigate the dynamic behavior of liquid water entering into PEFC gas channels from gas diffusion layer (GDL) pores [24]. This method needs to solve additionally a scalar transport equation for liquid volume fraction, and in order to accurately reconstruct the interfaces between single- and two-phase regions fine mesh is critically needed. The extremely intensive computational cost hinders its practical application to PEFC modeling. In the present work, a three dimensional transient model is developed using the M2 formulation. A salient feature of this model is the complete treatment of two-phase transport throughout a PEFC, including gas channels, thus enabling detailed studies on the liquid water formation, transport, and flooding in CLs, GDLs and channels, and furthermore the channel clogging and flow maldistribution.

This work focuses only on elucidating the liquid water motion in a single-channel PEFC with particular interest on the liquid water accumulation and transport in gas channels. In the next section is brought out a three dimensional, transient, non-isothermal, two phase flow PEFC model. The third section presents detailed simulation results and discussion. Major conclusions are then summarized in the final section.

2. The PEFC model

We consider a PEFC consisting of nine sub-regions: two flow plates in the anode and cathode respectively, an anode channel, an anode gas diffusion layer, an anode catalyst layer, an ionomeric membrane, a cathode catalyst layer, a cathode gas diffusion layer, and a cathode channel, as schematically shown in Fig. 1. No anode and cathode micro-pore layers are included, since of particular interest here is the liquid water accumulation and transport in gas channels and we do not want to get involved in the disputation [25–27] about the effects of micro- pore layers on PEFC performance. Humidified air and hydrogen are fed into the cathode and anode channels, respectively, in counter flow. A constant current density is prescribed at the outer surface of the cathode flow plate. Model development is based on the works by Wang and Wang [10,13]. The developed three dimensional PEFC model fully accounts for the transient transport and electrochemical processes with a complete treatment of two phase flow throughout the PEFC, and can be concisely summarized in the form of the following governing equations:

Continuity equation

$$\frac{\partial \rho}{\partial t} + \nabla \cdot \left(\rho \frac{\vec{u}}{\varepsilon} \right) = 0 \tag{1}$$

Momentum conservation equation

$$\frac{\partial (\rho \vec{u}/\varepsilon)}{\partial t} + \nabla \cdot \left(\frac{\rho \vec{u}\,\vec{u}}{\varepsilon^2} \right) = \nabla \cdot (\mu \nabla \vec{u}) - \nabla P + S_u \tag{2}$$

Energy conservation equation

$$\frac{\partial \left[\overline{\rho c_p} T \right]}{\partial t} + \nabla \cdot \left[\gamma_T \rho c_p \vec{u} T \right] = \nabla \cdot \left(k^{\mathrm{eff}} \nabla T \right) + S_T \tag{3}$$

Species conservation equation

$$\frac{\partial \left(\varepsilon^{\mathrm{eff}} C^i \right)}{\partial t} + \nabla \cdot \left(\gamma_C \vec{u} C^i \right) = \nabla \cdot \left(D_g^{i,\mathrm{eff}} \nabla C_g^i \right) - \nabla \cdot \left[\left(\frac{m f_l^i}{M^i} - \frac{C_g^i}{\rho_g} \right) \vec{j}_l \right] + S_C^i \tag{4}$$

Charge conservation (electrons) equation

$$0 = \nabla \cdot \left(\sigma_s^{\mathrm{eff}} \nabla \Phi_s \right) + S_{\phi_s} \tag{5}$$

Charge conservation (protons) equation

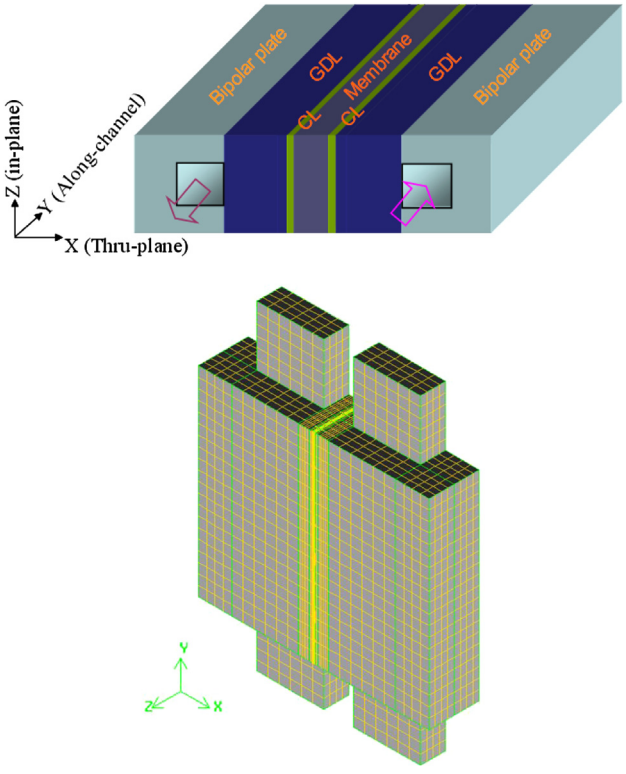

Fig. 1 – Geometry and mesh of a single-channel PEFC.

Table 1 – Source terms for the conservation equations in different sub-regions.

	S_u	S_T	S_C^i	S_{φ_e}	S_{φ_s}
Gas channels	$-\frac{\mu}{K_{GC}}\vec{u}$	$\dot{m}_{gl}h_{gl}$	0	–	0
GDLs	$-\frac{\mu}{K_{GDL}}\vec{u}$	$\frac{i_s^2}{\sigma_s^{eff}}+\dot{m}_{gl}h_{gl}$	0	–	0
CLs	$-\frac{\mu}{K_{CL}}\vec{u}$	$j\left(\eta+T\frac{dU_0}{dT}\right)+\frac{i_e^2}{\kappa_e^{eff}}+\frac{i_s^2}{\sigma_s^{eff}}+\dot{m}_{gl}h_{gl}$	$-\nabla\cdot\left(\frac{n_d}{F}i_e\right)-\frac{s_i j}{n_i F}$	j	$-j$
Membrane	–	$\frac{i_e^2}{\kappa_e^{eff}}$	–	0	–
Bipolar plates	–	$\frac{i_s^2}{\sigma_s^{eff}}$	–	–	0

Electrochemical reactions:

$\sum s_i M_i^z = ne^-$ where $\begin{cases} M_i: \text{ chemical formual of species } i \\ s_i: \text{ stoichiometry coefficient} \\ n: \text{ number of electrons transferred} \\ z: \text{ charge number} \end{cases}$

In PEFCs, there are:

(anode) $H_2 - 2H^+ = 2e^-$

(cathode) $2H_2O - O_2 - 4H^+ = 4e^-$

Note: n_d is the electro-osmotic drag coefficient for water. For H_2 and O_2, $n_d = 0$.

$$0 = \nabla\cdot\left(\kappa_e^{eff}\nabla\Phi_e\right)+S_{\phi_e} \tag{6}$$

where $\vec{u}$, P, T, C^i, Φ_s, and Φ_e are the primary variables to be solved, denoting the superficial fluid velocity vector, pressure, temperature, molar concentration of species i, electronic phase potential, and electrolyte phase potential, respectively. Major assumptions of the present model are summarized as follows [10,13]: (i) ideal gas mixture; (ii) isotropic and homogeneous membrane, catalyst layers, and gas diffusion layers; (iii) incompressible and laminar flow; (iv) negligible mass source/sink in the continuity equation, i.e. Eq. (1); (v) negligible electrochemical double layer effect on charge transport; and (vi) water vapor interfacial equilibrium during transient phase change. Water transport through the membrane relies on molecular diffusion, electroosmotic drag, and hydraulic permeation while the membrane water absorption/desorption that may play some role [28] for the overall water transport through the membrane is not taken into account. Constitutive relationships related to the complete treatment of two phase flow throughout the cell, of main interest in the present work, are elaborated below.

The gas channels are looked as structured and ordered porous medium [14] like the porous diffusion media, the source term (S_u) in the momentum equation, Eq. (2), is thus formulated as

$$S_u = \begin{cases} -\frac{\mu}{K_{GC}}\vec{u} & \text{in gas channels} \\ -\frac{\mu}{K_{GDL}}\vec{u} & \text{in GDLs} \\ -\frac{\mu}{K_{CL}}\vec{u} & \text{in CLs} \end{cases} \tag{7}$$

The porosity in gas channels equals to unity and the permeability (K_{GC}) is obtained from the hydraulic conductance of laminar single-phase Hagen–Poiseuille flow, as [14]

$$K_{GC} = c\frac{d_h^2}{32} \tag{8}$$

where, d_h is the hydraulic diameter of the gas channel and c is a shape factor related to the cross-sectional shape of the channel.

Dynamic viscosity (μ) and density of the two phase mixture are defined respectively as

$$\mu = \rho\left(\frac{k_{rl}}{\nu_l}+\frac{k_{rg}}{\nu_g}\right)^{-1} \tag{9}$$

$$\rho = s\rho_l+(1-s)\rho_g \tag{10}$$

Here, the liquid saturation (s) physically means the volume fraction of open pores occupied by liquid water. In the M2 regime, the liquid saturation is calculated from the mixture water molar concentration, C^{H_2O}, which is obtained by solving Eq. (4)

$$s = \frac{C^{H_2O}-C_{g,sat}^{H_2e}}{\rho_l/M^{H_2O}-C_{g,sat}^{H_2O}} \tag{11}$$

A complete treatment of the heat source term (S_T) in Eq. (3) yields

$$S_T = \begin{cases} j\left(\eta+T\frac{dU_0}{dT}\right)+\frac{i_e^2}{\kappa_e^{eff}}+\frac{i_s^2}{\sigma_s^{eff}}+\dot{m}_{gl}h_{gl} & \text{in CLs} \\ \frac{i_e^2}{\kappa_e^{eff}} & \text{in membrane} \\ \frac{i_s^2}{\sigma_s^{eff}}+\dot{m}_{gl}h_{gl} & \text{in GDLs} \\ \frac{i_s^2}{\sigma_s^{eff}} & \text{in bipolar plates} \\ \dot{m}_{gl}h_{gl} & \text{in gas channels} \end{cases} \tag{12}$$

where h_{gl} denotes the latent heat of vapor–liquid phase change and $\dot{m}_{gl}$ is the phase change rate, which is determined from the liquid continuity equation as

$$\dot{m}_{gl} = \rho_l\frac{\partial s}{\partial t}+\nabla\cdot(\rho_l\vec{u}_l) \tag{13}$$

In the M2 regime, the liquid velocity ($\vec{u}_l$) is computed from

$$\rho_l\vec{u}_l = \vec{j}_l+\lambda_l\rho\vec{u} \tag{14}$$

with the capillary diffusion flux $\vec{j}_l$ being calculated by

$$\vec{j}_l = \frac{\rho\lambda_l\lambda_g}{\mu}K\nabla P_c \tag{15}$$

where, the relative mobilities of individual phases, λ_l and λ_g are respectively calculated by

Table 2 – Geometrical parameters, operating conditions and material properties.

Quantity	Value
Gas channel depth/width	0.75/1 mm
BP shoulder width	0.5 mm
Anode/cathode GDM thickness	200/200 μm
Anode/cathode CL thickness	10/10 μm
Membrane thickness	30 μm
Cell height/length	1.5/300 mm
Anode/cathode pressure	2.0/2.0 atm
Cell operating temperature	353.15 K
Dew point of anode/cathode inlet gas	343.15/343.15 K
Current density	800 mA cm^{-2}
Anode/cathode stoichiometry	2.0/2.0
Anode/cathode inlet gas temperature	353.15 K
Temperature at the outer surface of anode/cathode BP	353.15/353.15 K
Porosity in GDL/CL	0.65
Porosity in gas channels	1.0
Volume fraction of ionomer in CL	0.25
Permeability in GDL/CL	1.0×10^{-12} m^2
Permeability in gas channels	0.33×10^{-7} m^2
Contact angle in GDL/CL	92°
Contact angle in gas channels	60°
Membrane hydraulic permeability	5.0×10^{-20} m^2
Heat capacity of membrane	1650 kJ m^{-3} K^{-1}
Heat capacity of CL/GDL/bipolar plate (solid component)	3300/568/1580 kJ m^{-3} K^{-1}
Specific heat of fluid mixture	2000 J kg^{-1} K^{-1}
Effective heat conductivity in membrane/CL/GDL/bipolar plate	0.95/2.94/10/20 W m^{-1} K^{-1}
Latent heat of vapor condensation	2.27×10^6 J kg^{-1}
Effective electronic conductivity in diffusion media/bipolar plate	3000/20,000 S m^{-1}
Equivalent weight of ionomers	1.1 kg mol^{-1}
Density of dry membrane	1980 kg m^{-3}

$$\lambda_l = \frac{k_{rl}/\nu_l}{k_{rl}/\nu_l + k_{rg}/\nu_g} \quad \text{and} \quad \lambda_g = 1 - \lambda_l \tag{16}$$

The relative permeabilities, k_{rl} and k_{rg}, in Eqs. (9) and (16) are defined, respectively, as the ratio of intrinsic permeability of liquid and gas phases to the total intrinsic permeability of a porous medium, which physically describe the extent of one phase being hindered by the other in pore spaces and thus can be formulated as a function of the liquid saturation, such that

$$k_{rl} = s^n \quad \text{and} \quad k_{rg} = (1-s)^n \tag{17}$$

Following the work by Luo et al. [12], the exponential n in Eq. (17) is taken to be 4.0 for two phase flow in the porous diffusion media, while in the gas channels we consider $n = 5.0$, which was recommended by the experimental validation conducted in Wang et al. [14].

All the source terms, S_u and S_T together with S_C^i, S_{φ_e}, and S_{φ_s}, are summarized in Table 1. The physical, transport and electrochemical properties, and more constitutive relationships of M2 model are the same as in Wang and Wang [10,13] and thus are not repeated in the present work. Geometrical parameters, operating conditions, and material properties of the PEFC are tabulated in Table 2.

The complete set of governing equations, Eqs. (1)–(6), contains nine unknowns: $\vec{u}$ (three components), P, T, C^{H_2} in the anode or C^{O_2} in the cathode, C^{H_2O} (or λ in the membrane), Φ_s, and Φ_e. Appropriate boundary and initial conditions are required to close this mathematical system.

Zero-flux boundary conditions are prescribed at all external boundaries for all the transport equations if not explicitly pointed out. Temperature at the outer surface of the anode/cathode flow plate is fixed at the cell operating temperature. For the electronic phase potential, a reference potential (zero) is set at the anode side and a constant flux (current density) I, 800 mA cm^{-2}, is prescribed at the outer surface of the cathode bipolar plate. At the channel inlets, the gas velocity $\vec{u}_{in}$ can be calculated from the stoichiometric flow ratio, i.e. ξ_a or ξ_c, defined at the current density, I, namely

$$\xi_a = \frac{C^{H_2} u_{in,a} A_{in,a}}{\frac{IA}{2F}}, \quad \xi_c = \frac{C^{O_2} u_{in,c} A_{in,c}}{\frac{IA}{4F}} \tag{18}$$

The inlet gas temperature is set to be the cell operating temperature and the inlet species molar concentrations are calculated from the inlet pressure, temperature and humidity in terms of the ideal gas law. As the gas channels are looked as porous medium, the walls or interfaces between channel and BP are considered to be fully-slip.

The initial temperature throughout the cell is set uniformly at the cell operating temperature. The reactant species and water concentration in the gas channel and porous media are initially set to have the same molar concentrations as the corresponding inlet gas. The membrane is assumed to be water-saturated ($\lambda = 14$) initially. The initial electronic phase potential is specified to be zero in the anode, while 0.79 V in the cathode.

The conservation equations together with the appropriate boundary/initial conditions are solved in the commercial CFD flow solver, Fluent® (version 6.3.26). By customizing its User Defined Functions (UDF), various source terms, physical properties, and non-standard advection-convective terms in the governing equations, Eqs. (1)–(6), are implemented. The well-known SIMPLE (semi-implicit method for pressure linked equation) algorithm is used to address the pressure–velocity coupling and the first order upwind differencing scheme is used for the discretization of velocity field. To accelerate convergence, the AMG (algebraic multi-grid) iterative method is applied to solve the linearized algebraic equations. A fully implicit scheme is used to discretize the transient terms in order to maximize the time step and reduce the calculation time. Overall species imbalances at every time step together with the equation residuals are used as important convergence criteria to ensure physics-meaningful results. The transient calculation is terminated once all the variables remain almost unchanged – reaching the steady operation. The numerical mesh has been sketched in Fig. 1. The symmetry with respect to the middle X–Y plane (see Fig. 1) allows the numerical simulation to be carried out only in the upper-Z half of the single-channel PEFC.

3. Results and discussion

The simulated unit cell is of active area 4.5 cm^2 (0.3 m × 1.5 mm) and operated at 200 kPa (absolute), 80 °C and

at 0.8 A cm^{-2}. Hydrogen and air both with dew point of 70 °C are fed into the anode and cathode respectively in counter flow. Stoichiometries at the anode and cathode side are both 2.0. Initially the MEA is assumed to be water-saturated.

The simulated evolution curve of the membrane protonic resistance, indicative of the hydration of membrane, is displayed in Fig. 2 together with the cell voltage curve. Upon loading, the membrane resistance increases as the initially water-saturated membrane is suddenly dried by the under-saturated reactant gases. Afterward it monotonously decreases, signifying a gradual hydration of the membrane by the water product due to ORR. After loading, the cell voltage is seen to increase first then gradually decrease. The cell voltage increase is a result of the membrane hydration, indicating the cell performance during this period is controlled by the Ohmic loss. Along with the formation of liquid water, flooding effects come into play and thus lead to the decrease of cell voltage. As evident from Fig. 2, after loading the decrease of membrane resistance exhibits three distinct stages, characterized by distinctly different slopes at the evolution curve. This is related to the evolution of liquid water in the PEFC electrodes to be presented next.

Fig. 3 shows the evolution curves of volumetrically averaged liquid water saturation in each sub-region of the PEFC. Liquid saturations in the CL and GDL in both the anode and cathode are all seen to fast increase, mildly increase and then gradually stabilize with time. Since the liquid saturation level in the electrodes is associated with the membrane hydration, the three distinct stages observed at the membrane resistance evolution curve (see Fig. 2) thus get explanation. As the water-generating electrode, the cathode generally has more liquid water presented. Nevertheless, liquid water appears in the anode gas channel shortly after loading, while it cannot be seen in the cathode channel until ~60 s into the operation. The fast accumulation of liquid water in the cathode gas channel greatly slows down the increase of liquid water in the other sub-regions. After ~410 s into the operation, liquid water in the cathode channel becomes stabilized and the system gradually approaches the final steady state. The evolution curve of liquid water in the anode gas channel features always a gradual increase with time throughout the operation. Even at the end of simulation time (716 s), a slight increase of liquid saturation in the anode channel is still seen. Different mechanisms for liquid water accumulation and transport in the anode and cathode gas channels must be involved.

Evolution of the profiles of cross-section averaged liquid water saturation in the gas channels is shown in Fig. 4. Liquid water first appears in the mid-Y regions and the onset of liquid water in the anode channel is much earlier than in the cathode channel. From Fig. 4b, it is seen that liquid water is building up toward the cathode channel exit. At 416 s into the operation, the buildup of liquid water in the cathode channel is almost completed. Liquid saturation in the cathode channel can reach slightly higher than 20% in the channel outlet region. As displayed in Fig. 4a, liquid water in the anode gas channel exhibits a peak value in the mid-Y region. The decrease of liquid water toward the anode channel exit is due

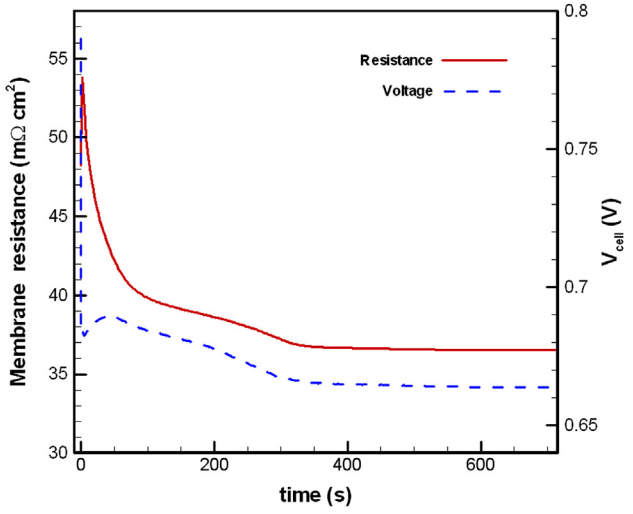

Fig. 2 – Evolution curves of the membrane proton resistance and cell voltage.

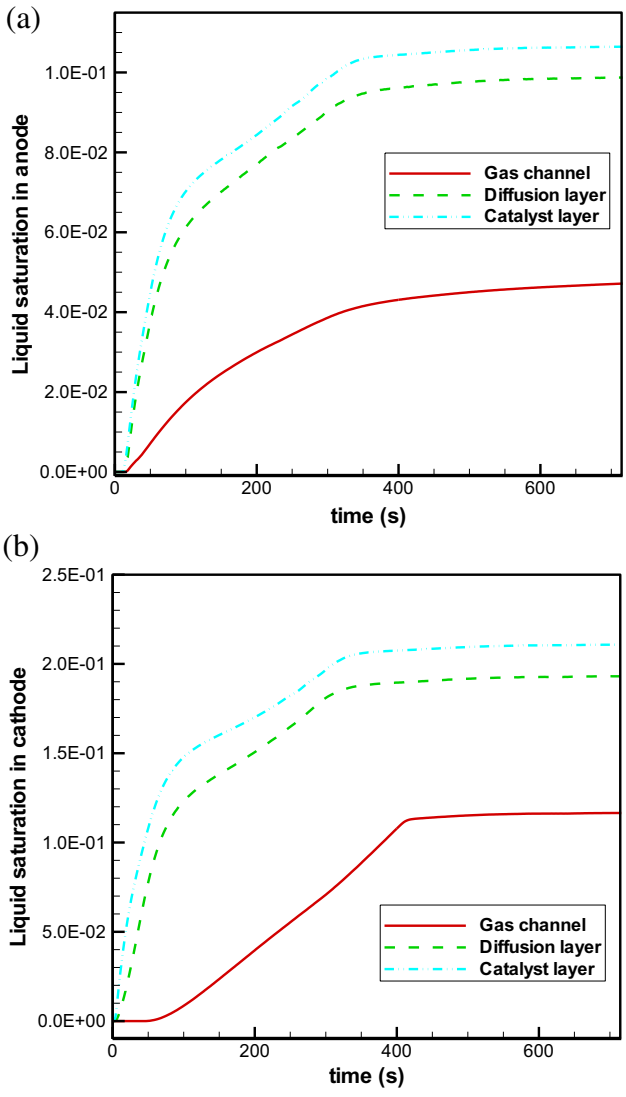

Fig. 3 – Evolution curves of volumetrically averaged liquid saturation in each sub-region (a) in the anode and (b) in the cathode.

to the evaporation of liquid water into the surrounding gas. Although the peak value of liquid saturation in the anode gas channel can be as high as ~10%, liquid saturation at the channel exit remains below 2%.

The buildup of liquid water in the cathode gas channel dominates the liquid water evolution inside the cell and further dictates the cell performance. Figs. 2 and 3 both indicate that the system needs ~400 s to get stabilization, which is actually because that the complete buildup of liquid water in the cathode channel takes around ~416 s (see Fig. 4b).

To explore the liquid water motion inside the PEFC in detail, evolution of the liquid saturation distribution at specified plane is monitored. Results at two planes, one is the mid-Z symmetric plane (Z = 0) and the other the cross-sectional plane at Y = 0.2 m (refer to Fig. 1 for the geometry and coordinate system), are displayed in Figs. 5 and 6, respectively. (Please note that all the plots in Figs. 5–8 are drawn not to scale for better view.) The formation and transport of liquid water in the entire PEFC are clearly seen from these two figures.

Seen from Fig. 5, in the cathode, liquid water first appears in the catalyst layer in the mid-Y part of the cell then gradually spreads to the other sub-regions. There exists always a negative liquid saturation gradient in the through-plane direction (X) which drives the liquid water from the cathode CL, across the GDL, and into the gas channel. The cathode gas has relatively larger density and faster flow velocity. The liquid water accumulated in the cathode gas channel is thus dragged by the gas and gradually moves toward the exit. At ~400 s into the operation (refer to Figs. 3b and 4b for quantitative data), the liquid water begins to flow outside from the exit along with the exhaust gas, stabilizing the liquid water in the cell and gradually resulting in the final steady state. Due to the dragging effect of the cathode gas, the region with the largest liquid saturation in the cathode is seen to shift toward the channel exit with time.

From Fig. 5, we also see the liquid water is accumulating in the anode. In contrast, liquid water is first seen in the anode gas channel and no an explicit positive liquid saturation gradient exists in the through-plane direction, indicating the distribution of liquid water in the anode is virtually due to vapor condensation. Since the density of anode gas is relatively smaller and the flow velocity is relatively slower, the anode gas is not able to flush out the liquid water in the gas channel. The liquid water accumulated in the channel resides therein and the transport can only rely on a condensation–evaporation mechanism, which is in sharp contrast to the hydrodynamic transport of liquid water in the cathode gas channel.

The current collector is cooler than the adjoining porous medium. The saturated vapor transport driven by thermal gradient in the in-plane direction induces the so-called heat pipe effect [13] and more liquid water will form in the regions

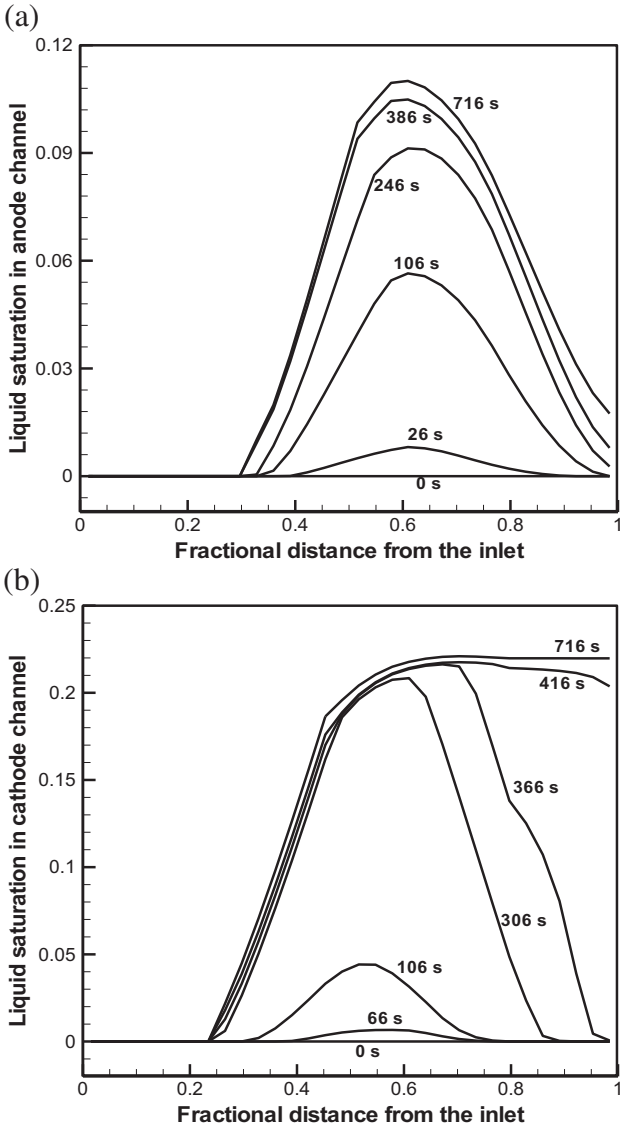

Fig. 4 – Buildup of liquid water in the (a) anode and (b) cathode gas channel.

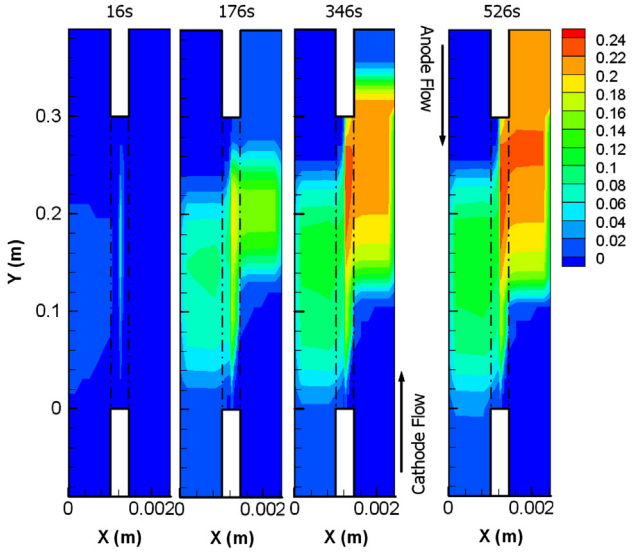

Fig. 5 – Liquid saturation distributions at time instants of 16 s, 176 s, 346 s and 526 s at the mid-Z symmetric plane (Z = 0). Note: the region surrounded by dash-dotted lines denotes the gas diffusion media and MEA; bipolar plates are not displayed in these plots.

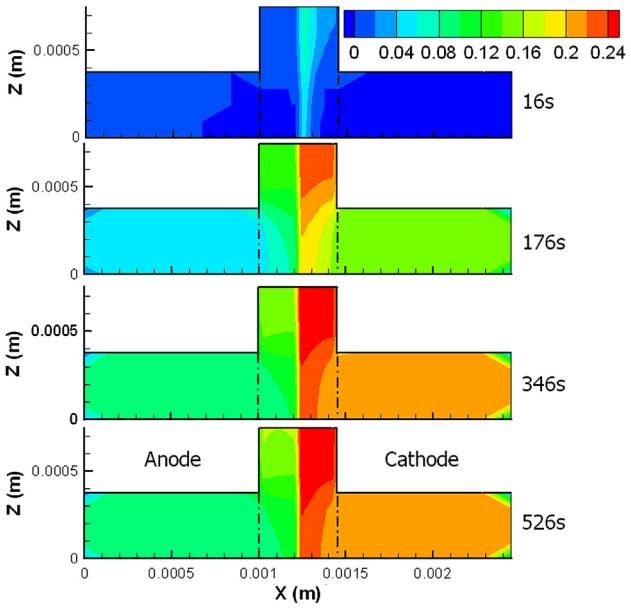

Fig. 6 – Liquid saturation distributions at time instants of 16 s, 176 s, 346 s and 526 s at the cross-sectional plane of Y = 0.2 m. Note: the dash-dotted lines indicate the interfaces between gas diffusion layers and channels; bipolar plates are not displayed in these plots.

underneath the land, as displayed by the plots in Fig. 6. In the cathode, liquid water saturation contours always exhibit a positive liquid saturation gradient in the in-plane direction (Z) and a negative liquid saturation gradient in the through-plane direction, indicating capillary diffusive transport is the dominant mechanism for liquid water transport in the cathode. However, in the anode, as evident by the contour plots at time instants of 346 s and 526 s, the liquid saturation at the land/GDL interface is higher than (or comparable to) that in the catalyst layer, indicating the condensation plays a major role for the liquid water accumulation/transport in the through-plane direction in the anode. The capillary diffusive transport still contributes to the liquid water distribution in the anode as a positive liquid saturation gradient is seen in the in-plane direction.

To shed more light on the liquid water accumulation in the gas channels, two monitoring planes are set at the interface of gas channel and GDL in the anode and cathode, respectively. Liquid saturation distributions at these two planes provide informative hints about how the liquid water enters the gas channel and where the liquid water comes from. Results are displayed in Figs. 7 and 8, respectively. Note that in all the plots of these two figures Z = 0 indicates the position of the mid-Z symmetric plane and Z = 0.375 mm denotes the top edge of the gas channel, above which is the land/GDL interface.

On the anode channel/GDL interface, the liquid water saturation is always higher in the high-Z locations, as displayed in Fig. 7, indicating most of the liquid water entering into the channel comes originally from the under-land region. That is to say, vapor condenses in the under-land region, then flows along the negative-Z direction and finally enters into the channel across the channel/GDL interface.

The liquid water accumulation in the cathode gas channel experiences different scenarios. The first two plots in Fig. 8 exhibit similar pattern as the plots in Fig. 7, implying during the early long period (~180 s) the liquid water entering into the cathode gas channel virtually origins from the vapor condensation in the under-land region. However, the last two plots in Fig. 8 show the liquid saturation in the low-Z part of the interface can be greater than that at the high-Z locations. A different mechanism for the liquid water accumulation in the cathode channel comes into play. The liquid water entering into the cathode channel comes directly from the GDL under-channel region. That is to say, the capillary diffusive transport transfers liquid water from the cathode CL, across the porous diffusion media, and into the gas channel.

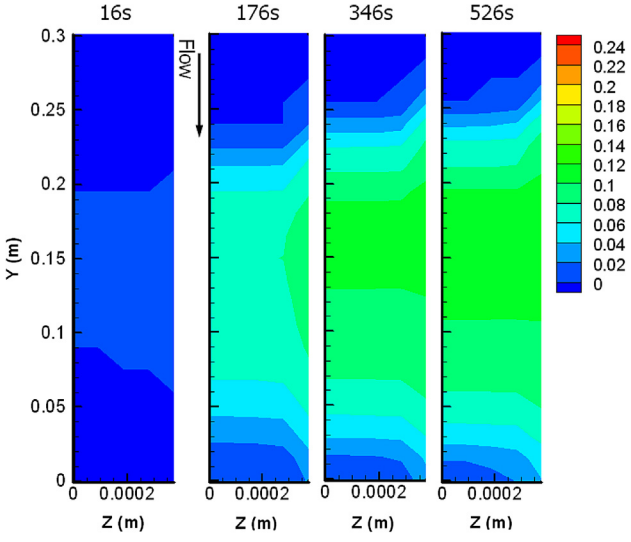

Fig. 7 – Liquid saturation distributions at time instants of 16s, 176 s, 346 s and 526 s at the interface of anode gas channel and gas diffusion layer.

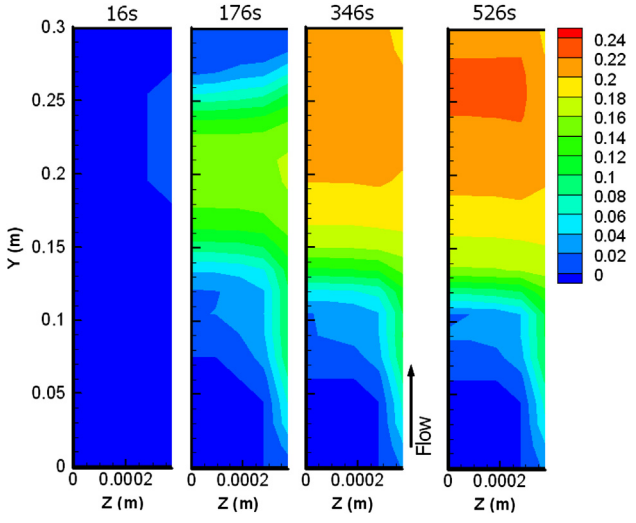

Fig. 8 – Liquid saturation distributions at time instants of 16 s, 176 s, 346 s and 526 s at the interface of cathode gas channel and gas diffusion layer.

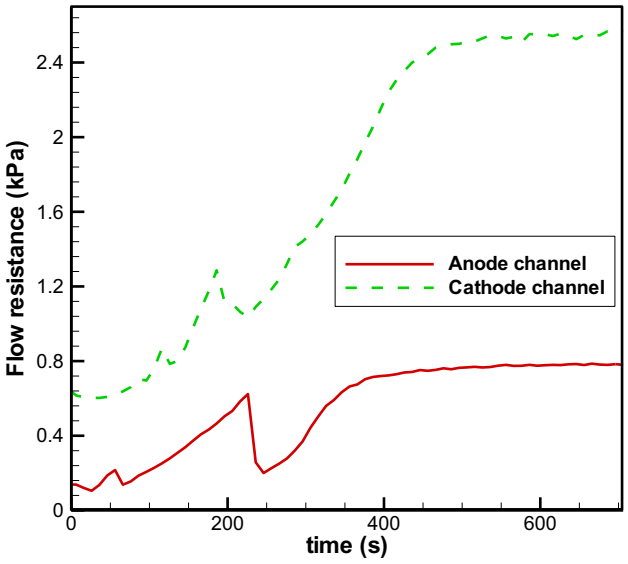

Fig. 9 – Evolution curves of flow resistance along the anode and cathode gas channels.

This mechanism for the liquid water accumulation in the cathode channel can finally take over the dominant role, as indicated by the last plot of Fig. 8.

Flow resistance along the channel is important to PEFC operations not only because it is directly related to the external energy consumption, but also provides ample information about the operational status. Abnormally large flow resistance may be indicative of channel clogging and/or flow maldistribution (for PEFC stack), which lead to operational instability and efficiency loss. The model developed in this work applies the two phase M2 theory throughout the PEFC, including gas channels, enabling the prediction of flow resistance along the gas channels. Fig. 9 displays the flow resistances along the anode and cathode gas channels as a function of time. It is seen that flow resistances fluctuate, and then significantly increase with time - the final stabilized flow resistances are ~2–3 times larger than the values in the very early period. Liquid water accumulation in the gas channel causes disturbances upon the flow and the flow resistance is thus seen to fluctuate. The presence of liquid water in gas channels alters the flow regime involved, from the single-phase homogeneous flow to two-phase flow. It is the alteration of flow regime that significantly increases the flow resistance.

4. Conclusions

Former PEFC models based on the M2 framework are generally lack of the capability for simulating the two phase flow in gas channels. In this work a three dimensional transient PEFC model is developed with a complete application of the two phase M2 theory throughout a PEFC, including gas channels, enabling detailed studies on the liquid water formation, transport, and flooding in the catalyst layers, porous diffusion layers and channels, and furthermore channel clogging and flow maldistribution.

This work focuses on elucidating the liquid water motion in the entire PEFC in general, and the liquid water accumulation and transport in gas channels in particular. Simulation with respect to a unit cell finds that the liquid water buildup in the cathode channel dominates the liquid water evolution inside the cell and further dictates the cell performance. It is also revealed from the simulation that the liquid water accumulation in gas channels relies mainly on three mechanisms: i) direct vapor condensation in the gas channel or at the BP wall; ii) vapor condensing into liquid at the BP/GDL interface and then being transported into the gas channel; iii) liquid water being directly transported into the gas channel from GDL. As the water-generating electrode, the cathode has more liquid water presented. The liquid water accumulation in the cathode gas channel relies mainly on mechanisms ii) and iii). The anode side exhibits a slightly lower temperature and condensation is thus found to play a dominant role for the liquid water distribution and transport in the anode. The liquid water accumulation in the anode gas channel relies mainly on mechanisms i) and ii). Due to the slow gas velocity and smaller gas density, the liquid water residing in the anode gas channel can rarely reach the outlet. Thus the transport of liquid water in the anode channel basically follows a condensation–evaporation mechanism, in sharp contrast to the hydrodynamic transport of liquid water in the cathode gas channel. The liquid water in the cathode channel can finally flow outside from the exit along with the exhaust gas. As the presence of liquid water in gas channels alters the flow regime involved, from the single-phase homogeneous flow to two-phase flow, the flow resistance is found to significantly increase.

Acknowledgments

Financial support of this work by ECEC sponsors is gratefully acknowledged. One of the authors, Dr. Fangming Jiang personally thanks the financial support received from the CAS “100 Talents” Plan.

List of symbols

A	area, m^2
c_p	specific heat, J kg^{-1} K^{-1}
C	species concentration, mol m^{-3}
D	species diffusivity, m^2 s^{-1}
F	Faraday constant, 96487 C/equivalent
h	latent heat of vapor condensation, J kg^{-1}
i	superficial current density, A m^{-2}
I	current density, A m^{-2}
j	capillary diffusive flux, kg m^{-2} s^{-1}; transfer current density, A m^{-3}
k	heat conductivity, W m^{-1} K^{-1}
k_r	relative permeability
K	permeability, m^2
mf	mass fraction
$\dot{m}$	phase change rate, kg m^{-3} s^{-1}
M	molar mass, kg mol^{-1}
P	pressure, Pa

s	liquid water saturation
S	source/sink
t	time, s
T	temperature, K
u	superficial fluid velocity, m s^{-1}
U_0	equilibrium potential, V
V_{cell}	cell voltage, V

Greek

ε	porosity or volume fraction
ϕ	phase potential, V
γ	advection correction factor for species transport
η	surface overpotential, V
κ	proton conductivity, S m^{-1}
λ	membrane water content, mol H_2O/mol SO_3^-; mobility of a certain phase
μ	dynamic viscosity, Pa s
ν	kinematic viscosity, m^2 s^{-1}
ρ	density, kg m^{-3}
σ	electronic conductivity, S m^{-1}
ξ	stoichiometric flow ratio

Subscripts and superscripts

a	anode
c	cathode; capillary
C	species
e	electrolyte
eff	effective
g	gas phase
gl	vapor–liquid phase transition
i	species id
in/out	channel inlet/outlet
l	liquid phase
s	solid phase; electron
sat	saturated value
T	heat
u	momentum
–	average
ϕ_e/ϕ_s	electrolyte/electron potential
→	vector

REFERENCES

[1] Yang XG, Zhang FY, Lubaway A, Wang CY. Electrochem Solid-state Lett 2004;7:A408–11.
[2] Zhang FY, Yang XG, Wang CY. J Electrochem Soc 2006;153:A225–32.
[3] Ge S, Wang CY. J Electrochem Soc 2007;154:B998–1005.
[4] Zhan ZG, Wang C, Fu WG, Pan M. Int J Hydrogen Energy 2012;37:1094–105.
[5] Lee D, Bae J. Int J Hydrogen Energy 2012;37:422–35.
[6] Patterson TW, Darling RM. Electrochem Solid-state Lett 2006;9:A183–5.
[7] Rangel CM, Silva RA, Travassos MA, Paiva TI, Fernandes VR. Fuel starvation: irreversible degradation mechanisms in PEM fuel cells. In: Stolten D, Grube T, editors. Proceedings of the 18th world hydrogen energy conference. Forschungszentrum Jülich GmbH; 2010. pp. 31–6.
[8] Pasaogullari U, Wang CY. J Electrochem Soc 2005;152:A380–90.
[9] Meng H, Wang CY. J Electrochem Soc 2005;152:A1733–41.
[10] Wang Y, Wang CY. J Electrochem Soc 2006;153:A1193–200.
[11] Ju H, Luo G, Wang CY. J Electrochem Soc 2007;154:B218–28.
[12] Luo G, Ju H, Wang CY. J Electrochem Soc 2007;154:B316–21.
[13] Wang Y, Wang CY. J Electrochem Soc 2007;154:B636–43.
[14] Wang Y, Basu S, Wang CY. J Power Sources 2008;179:603–17.
[15] Basu S, Wang CY, Chen KS. J Fuel Sci Technol 2009;6: 031007-1-11.
[16] Wang CY, Cheng P. Int J Heat Mass Transfer 1996;39:3607–18.
[17] Berning T, Djilali N. J Electrochem Soc 2003;150:A1589–98.
[18] Birgersson E, Noponen M, Vynnycky M. J Electrochem Soc 2005;152:A1021–34.
[19] He G, Ming P, Zhao Z, Abudula A, Xiao Y. J Power Sources 2007;163:864–73.
[20] Liu X, Lou G, Wen Z. J Power Sources 2010;195:2764–73.
[21] Sahraoui M, Bichioui Y, Halouani K. Int J Hydrogen Energy 2013;38:8524–31.
[22] Qin CZ, Rensink D, Fell S, Hassanizadeh SM. J Power Sources 2012;197:136–44.
[23] Quan P, Lai MC. J Power Sources 2007;164:222–37.
[24] Zhu X, Liao Q, Su PC, Djilali N. J Power Sources 2010;195:801–12.
[25] Lee J, Hinebaugh J, Bazylak A. J Power Sources 2013;227:123–30.
[26] Owejan JP, Owejan JE, Gu W, Trabold TA, Tighe TW, Mathias MF. J Electrochem Soc 2010;157:B1456–64.
[27] Passaogullari U, Wang CY, Chen KS. J Electrochem Soc 2005;152:A1574–82.
[28] Majsztrik PW, Satterfield MB, Bocarsly AB, Benziger JB. J Membrane Sci 2007;301:93–106.